The Indices of Refraction of SiO_2 and AlF_3 in the XUV Determined from Simultaneous Reflection and

Transmission Measurements on XUV Diodes

Brooke Croxall

A Senior Thesis submitted to the faculty of

Brigham Young University

In partial fulfillment of the requirements for the degree of

Bachelor of Science

R. Steven Turley and David D. Allred, Advisors

Department of Physics and Astronomy

Brigham Young University

April 13, 2022

Abstract

The Indices of Refraction of SiO_2 and AlF_3 in the XUV Determined from Simultaneous Reflection and
Transmission Measurements on XUV Diodes

Brooke Croxall
Department of Physics and Astronomy, BYU
Bachelor of Science

I studied angular-dependent extreme ultraviolet (XUV) transmission and reflection data from an XUV-absolute photodiode to obtain indices of refraction of the diode's surface SiO_2.layer. These parameters were also measured for an aluminum fluoride thin film which covered half the diode's surface. Measurements were made at the Advanced Light Source (ALS) by BYU students. Various multilayer optical models were explored to extract the thickness of the AlF_3 and SiO_2 layers and the indices of refraction of SiO_2. This study looked at wavelengths from 12 nm to 49.5 nm. I found the indices of refraction SiO_2 to be close to the literature values at the shorter wavelengths (up to about 20 nm) but then the indices of refraction increasingly deviated as the wavelengths approached the upper limit of wavelengths measured—49.5 nm.

Acknowledgements

I would like to acknowledge Dr. R Steven Turley who took me under his wing to teach me so much about thin film optics.

I want to give a special thanks to Dr. David Allred for helping me finish and revise my report after Dr. Turley retired. He spent many hours with me making this paper what it is.

Thank you to the members of the XUV-Thin Film Research Group for the support.

Table of Contents

List of Figures

Chapter 1: Introduction

1.1 Background

1.1.1 Aluminum Coated Broadband Mirrors

To expand the abilities of space exploration, there is a need of a wider range of reflectance of telescope mirrors. Telescopes need broadband mirrors which have close to total reflection over a wide range of wavelengths. These broadband mirrors have a metallic coating whose properties lead to high reflection of light over a wide spectral range [1]. Examples of some common coatings for mirrors and their reflectance are shown in Fig. 1.
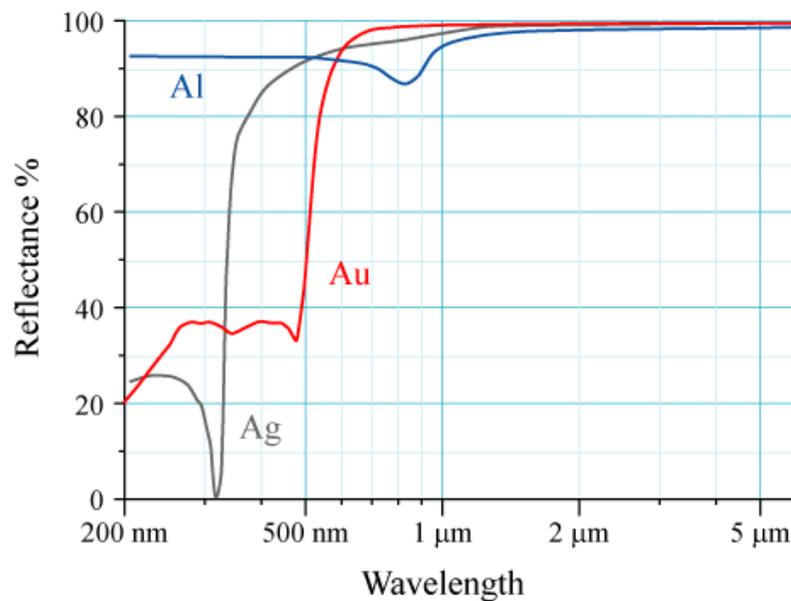
Fig. 1.   Reflectance Spectrum of gold, aluminum, and silver at normal incidence [2].

As can be seen in Fig. 1, aluminum is the only element that has reflection of over 85% from 200 nm to 5 µm. Other coatings such as gold and silver have very low reflectance, below 40%, at shorter wavelengths. Because of this wide range of high reflectance, aluminum has proven to be an effective coating on broadband mirrors for the use of telescopes. The disadvantage of bare aluminum is that it readily oxidizes. This leads to a drastic reduction of the reflectivity in the vacuum ultraviolet. Even an Al_2O_3 coat that is only about 3 nm thick causes a significant decrease in reflectivity below 149 nm [3]. To try to counteract the effects of oxidation, a metallic fluoride with wide bandgap can be used as an oxidation barrier which can be placed on top of the aluminum mirror which can decrease the effects of oxidation [4]. Aluminum fluoride shows promising ability to oppose the effects of oxidation as a barrier coating. To further implement the use AlF_3 as an oxidation barrier its optical properties must be verified, modified, and updated.

1.1.2 Interest in the XUV

The extreme ultraviolet, or the XUV, is defined as the subsection of wavelengths of 10-100 nm in length within the ultraviolet range shown in the dark purple region in Fig. 2. This range is particularly important in the exploration of space study and for the use of space telescopes. When a telescope can reflect a wider the range of wavelengths, there is a greater ability to characterize interstellar bodies and phenomena in space. Interstellar bodies or parts of bodies that emit most of their radiation in the ultraviolet are very hot compared to bodies giving off mostly infrared and visible light. Examples of phenomenon that give off extreme ultraviolet radiation are solar flares and stars and galaxies at the beginning and end of their lives [5]. With wider range of reflectance these instances of ultraviolet radiation can be further studied and located.

2

There is desire to improve the reflection of aluminum mirrors in the extreme ultraviolet. to have the ability to reflect the wavelengths in the extreme ultraviolet to expand visibility of these telescopes.
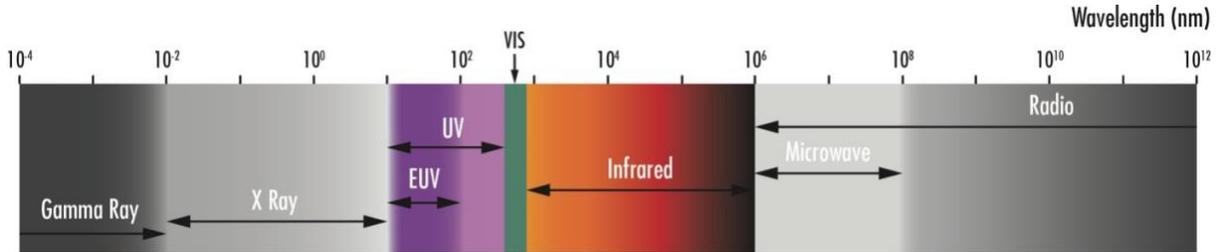
1.1.3 Aluminum Fluoride

These next generation telescopes will benefit from the use of aluminum-coated, advanced broadband mirrors which have high reflectance from the deep UV to infrared light [7], [8]. Since aluminum shows to be a good candidate as a metallic coating on broadband mirrors as described above but its oxidation causes a problem in the XUV, in this study I am specifically interested in the optical properties of AlF_3 thin films which can potentially serve as an oxidation barrier on these mirrors. Since the method of this study is using a silicon diode to measure reflectance and transmission of the thin films, the optical properties of SiO_2 must also be characterized in order to fully characterize the optical properties of AlF_3.

A reason AlF_3 could serve as a good oxidation barrier on aluminum coated mirrors is due to the chemical bond between aluminum and fluorine versus aluminum and oxygen. As shown in Fig. 3, the electronegativity of fluorine, with has symbol F, in the right corner has the highest electronegativity on the periodic table. Since fluorine is in the seventh row, it has seven valence electrons, which means it is very reactive. This means it easily reacts with other elements to fill its last orbital. In the context of AlF_3 as an oxidation barrier to reduce Al_2O_3 creation, fluorine

3

has a higher electronegativity than oxygen. Because of this higher difference in electronegativity, aluminum creates a stronger bond with fluorine than with oxygen [9]. Stronger bonds also correlate with less UV absorptions. So thin AlF3 films do not readily absorb radiation for wavelengths above 120 nm.

The earth's atmosphere blocks out most of the radiation that comes from the ultraviolet which means that to record emissions of these wavelengths' telescopes must be placed in space or the outer atmosphere [5]. By using AlF_3 as an oxidation barrier could keep the aluminum covering from oxidizing before it reaches oxygen-free space. Other metallic fluorides have been studied and used as these oxidation barriers such as MgF_2 and LiF where the same difference in electronegativity causing them to be good barriers since the electronegativity of fluorine is the highest on the periodic table.

Fig. 3.   Periodic table of electronegativity. Note the electronegativity of fluorine (F) in group 17 and period 2. Also note oxygen (O), which is directly to the right of fluorine. Used with permission [10].

1.1.4 Advanced Light Source Data Collection

The Advanced Light Source (ALS) at The Berkeley National Laboratory is a synchrotron that is made to accelerate electrons near the speed of light. An electron traveling near the speed of light in the synchrotron is constantly forced to change direction which leads to the emission of high energy radiation in the form of light at differing wavelengths [11], [12]. The ALS can produce different wavelengths from x-ray all the way to IR which is used in the 40 different beamlines. Each beamline has a diffraction grating to disperse the beam composed of many different wavelengths into its components. Different diffraction gratings have different number of number of lines per mm that can extract different lengths of wavelengths.

As can be seen in the schematic of the ALS in Fig. 4, it is circular to accelerate the electrons at extreme speeds so the XUV wavelengths can be emitted. The storage ring (labeled)

is very large to maintain the extremely high beam energy of 1.0 to 1.9 GeV and its circumference

is 196.8 m [13]. The beamlines carry the light and then have diffraction gratings and specific

instruments to use the light as desired [14]. At the end of the beamlines is where the users

interact and measure the light. This location is labeled as "Experiments" in Fig. 4. The data

collection method for this experiment is described in the methods chapter of this paper. This

study used beamline 6.3.2 which has energy ranging from 25-1300 eV which correlates to

wavelengths 10-500 Å. For more information about the specifications of the beamline used for

data collection in this study, see [15].
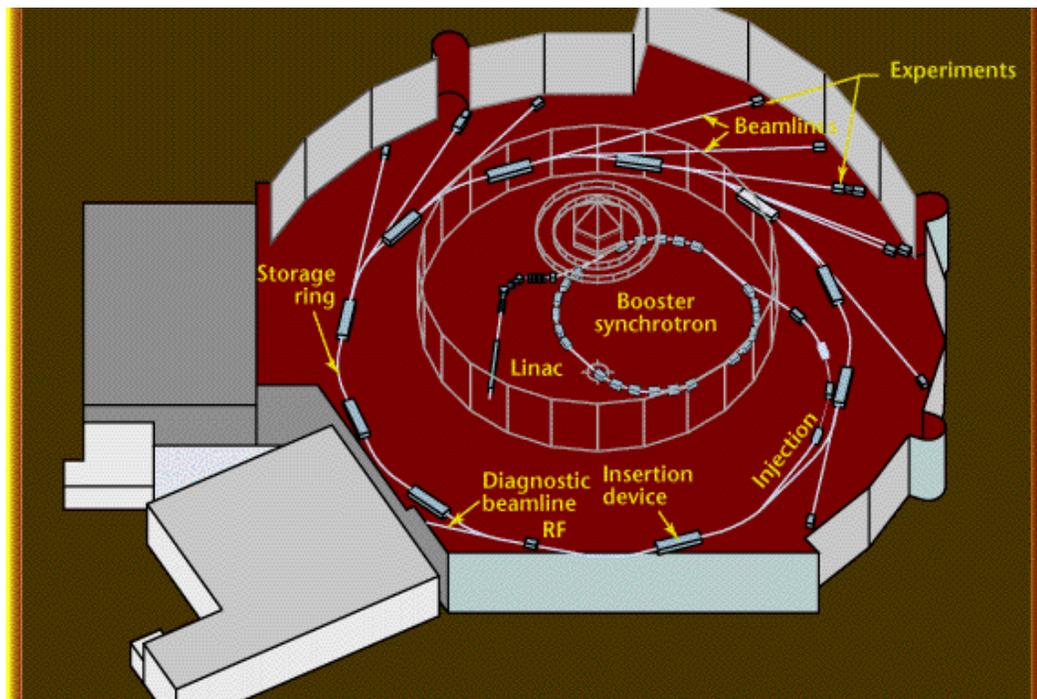
Fig. 4.   Diagram of the synchrotron at the Advanced Light Source in Berkeley, California. Used with permission [16].

1.2 Prior Work

There have been previous studies on certain aspects of the project I am conducting with

the simultaneous measurement of the optical properties of aluminum fluoride in the extreme

ultraviolet at BYU as well as outside.

One study conducted by John Hennessy had similar goals that looked specifically at optical properties of aluminum fluoride in the ultraviolet region. Like my project, both reflection and transmission data were used, but of wavelengths around 200 nm were studied which are longer wavelengths than I used to find the optical properties of AlF_3 [16]. I will be looking at wavelengths in the XUV from 5 nm to 50 nm.

1.2.1 Previous Work Done at BYU

For many years the XUV-Thin Film Research Group has been studying about optical properties of different film films, relating to the effects of humidity, measuring roughness, and other properties of the different materials for application on space telescopes [3]. There have been trends found where there have been discrepancies found in indices of refraction for AlF_3 and other compounds like SiO_2 derived from the literature.

Previous studies at BYU have looked at optical properties of different thin film layers such as yttrium oxide (Y_2O_3), LiF, and AlF_3 [17]. Margaret Miles conducted a master's thesis looking at how aluminum fluoride acts as a barrier layer on aluminum mirrors [18]. She found that a 2.4 nm AlF_3 layer on an aluminum mirror significantly retards the oxidation effects. While AlF_3 has been and is currently being studied, these studies do not use the simultaneous measurement of both reflection and transmission to measure the optical constants.

Kenan Fronk studied the effects of storing AlF_3 on top of aluminum mirrors because many times advanced broadband mirrors used for telescopes are stored for months before being sent in space. He found that the thickness of approximately 30 nm thick AlF_3 bilayer mirrors at 327 K in dry air did not change significantly over 2500 hours. This supports that AlF_3 can be a good coating for aluminum mirrors because the thickness does not change significantly over time [19].

Another undergraduate student at BYU, Alexandra Davis, showed that 9 nm of AlF_3 deposited on aluminum prevented the growth of oxidation for over 200 hours [20]. These past studies corroborate the fact that AlF_3 indeed is a good candidate as a coating on aluminum and should continue to be studied.

I will be using data taken by other students in the group to create models to find the index of refraction at different wavelengths. Other students in recent years have only focused on modeling reflection, while this study focuses on models of transmission of the ALS data to extract optical properties of AlF_3 in the XUV.

1.3 Purpose of Study

There have been many aspects of AlF_3 that have been studied by the XUV-Thin Film Research Group at BYU, but there are still optical properties of the index of refraction that are missing from the equation that is needed for full implementation of AlF_3 to be used on aluminum mirrors so the range of wavelengths needed for the specific telescope can be reached. While the original goal of this project was to characterize the index of refraction of AlF_3, the extent of this project was to quantify the thicknesses of the SiO_2 and Si layers as well as the indices of refraction of SiO_2 in the XUV range. This basis of the information of the diode are the beginning steps to further research for quantifying the indices of refraction of AlF_3 in this range of wavelengths. Since it appears that the values of the index of refraction of silica needs to be verified, characterizing the index of refraction of SiO_2 in the XUV is vital in the ability to use this method to further study AlF_3.

Chapter 2: Methods

In this chapter I will explain how the sample was prepared and the measurements I analyzed were made, as well as the models developed to find the thicknesses and indices of refractions of different wavelengths.

2.1 Sample Preparation

The sample I studied was an IRD absolute x-ray diode. It was half coated with a thin film of evaporated aluminum fluoride about 10 nm thick. The AlF_3 layer was deposited in a Veeco glass bell-jar thermal evaporator. An aluminum foil mask was used to block half the surface during the deposition. Three independent, resistance-heated evaporation sources were arrayed horizontally at the bottom of the chamber which allowed up to three different materials to be deposited without breaking vacuum. In this work only one source was used. The evaporator was equipped with an Inficon quartz-crystal thickness monitor (QCM) and manual shutters used to control film thicknesses. A sample platen was located about 30 cm above the evaporation sources. The platen was drilled like an optical breadboard with threaded holes spaced an inch apart in a square pattern to facilitate the attachment of the downward-facing samples to its underside. No sample rotation occurred as the sample stage was fixed for the duration of the deposition. The shutter was placed immediately below the substrate platen. It was controlled by a vertical rod attached to a rotational feedthrough in the base plate. In its closed position it blocks

atoms from all three sources, while in its open position, it allowed atoms from all sources to the reach the samples attached to the bottom of the substrate platen.

A substrate heater capable of reaching 520 K was constructed using four planar commercial 12 V heaters arranged side by side. The substrate heater assembly was hung by four long screws from the bottom of the platen leaving a space of 15 mm high between the top of the heaters and the platen. Aluminized insulation and aluminum foil was placed in the void to block heat transfer to the platen. Samples and a thermocouple were attached directly to the aluminum heaters to make good thermal contact. Aluminum fluoride chunks (99% purity) were placed in a tungsten evaporation boat (RD Mathis, Co). The chamber was evacuated to below 1×10^{-3} Pa and the substrate heater reached 490 K before evaporation commenced. The target AlF_3 evaporation rate was about 0.2 nm/sec. After the deposition the system was vented, the sample was removed and the AlF_3 thickness was determined via spectroscopic ellipsometry. The thickness of the oxide on the uncoated diode had been previously measured. Ellipsometry also established that the masked side was free of AlF_3.

2.2 Diode Measurements taken at the ALS

In recent years the XUV-Thin-Film Research Group has gone to the ALS to take measurements of thin films for use in research. With the synchrotron at the ALS as described in section 1.1.4, the XUV rays emitted from the diverted electrons provide the light to be measured in the device shown in Fig. 5.
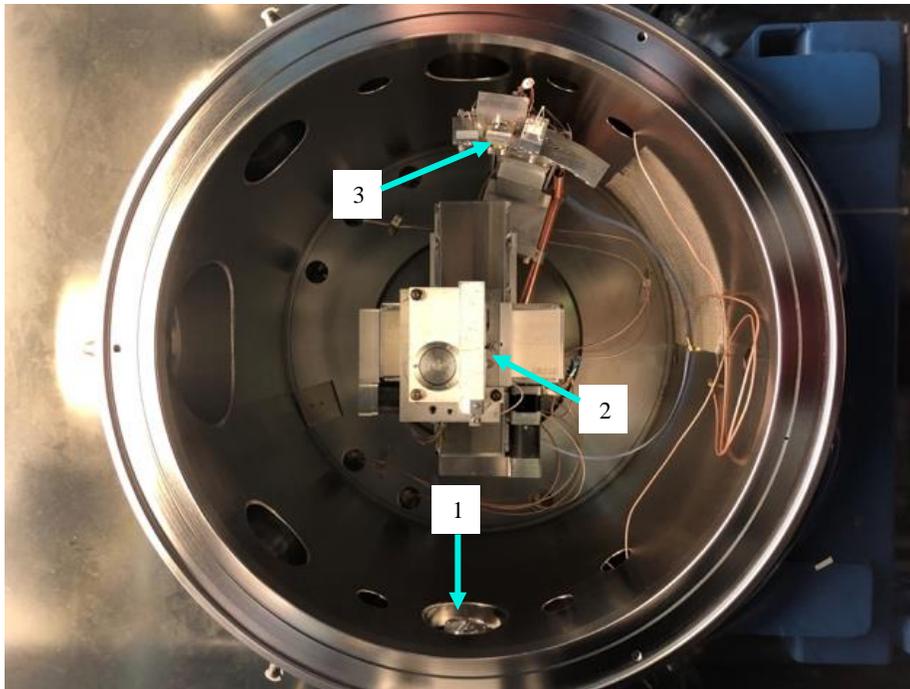
Key

1- XUV light enters
2- Thin film and diode location
3- Rotating arm holding detectors to measure reflection

Fig. 5.   Image of the system at the ALS used to take transmission and reflection data with the diodes. It is estimated to be about 75 cm in diameter. Source: Alexandra Gallion Shapley

At the bottom of the picture there is a hole, labeled 1, where the light enters. In measurements called $\theta - 2\theta$, both the transmission and reflection can be measured simultaneously. Theta is the angle that the light incident on the sample's surface makes relative to grazing incidence, while 2θ is twice that angle. This is the standard convention for x-ray measurements. At the chamber's center (number 2), at the optical axis lies the sample stage. The sample can be secured on it so that the top surface of the sample is on the optical axis. The x, y and z position of the sample stage can be manipulated remotely with stepper motors to position the part of the sample which is to be examined and to align its surface to grazing incidence at $\theta = 0$. The sample in this case is the half-coated, x-ray diode. Wires are attached to it so that the fraction of light that is transmitted into the active region of the diode can be measured. The reflectance detector (3) rotates around the optical axis (point two). It is placed at double the

sample angle, θ, to measure the specular reflection from the sample. This way, both transmission and reflection can be measured simultaneously. This system is about 2.5 feet in diameter.

2.3 Beer-Lambert Approximation

The first model that was used approximated the transmission through the AlF$_3$ to the diode. Beer's law is an estimation of the attenuation of light which can be used to model the transmission of thin films. Beer's Law is used many times in chemistry with different solutions. The most basic form says [21]

$$A = \varepsilon \ell c \tag{1}$$

Where A is the absorbance, ε is the molar attenuation coefficient, or the absorptivity ℓ is the optical path length, and c is the concentration of a solution. In the limit of a solid, the concentration is constant. The absorbance of the material is related to the

The Beer-Lambert law says

$$T = e^{-\kappa x} \tag{2}$$

Here κ is the absorption coefficient and x is the thickness through which the light passes (the optical path length). Applying this general formula to the data taken from the Advanced Light Source of extreme ultraviolet light going through a thin film and diode at different angles, the form used to model the data taken

$$\mathrm{T} = \exp\left(\frac{-\kappa \mathrm{d}}{\mathrm{f}(\theta)}\right) \tag{3}$$

Where, $f(\theta) = \sqrt{1 - \frac{n_1^2}{n_2^2}\cos^2\theta}$ and κ is the wavenumber times the imaginary part of the index of refraction. This is given by,

$$\kappa = \frac{4\pi \mathfrak{I}(n)}{\lambda} \tag{4}$$

12

This value is the absorption coefficient. The symbol λ is the wavelength and the d in Equation (3) is the thickness of the sample, which is constant for all the sample, but the distance the light travels depends on the angle, so it is divided by angle of incidence. $\Im(n)$ is the imaginary part of the index of refraction, called β hereafter. Since reflection is extremely high up to about 40 degrees, Beer's law leads to limitations on its accuracy of model below 40 degrees.

2.4 Hand Calculation of Transmission

After finding modeling different wavelengths with the Beer-Lambert Law, we wanted to check the accuracy of the model by comparing it to a hand calculation of a model of light passing through AlF_3 and SiO_2 by using Fresnel coefficients to calculate the s and p polarized light transmission through this interface. The initial model that was created, as shown in Fig 6., has three regions, the diode ambient (vacuum), a thin film of AlF_3, and lastly the top surface of the diode, which is SiO_2. Note that this model is incomplete as it does not take into account the top layer of Si under the SiO_2 that is electrical dead. The diode used, like semiconductor detectors in general, has a *dead layer* at its surface. Photons that are absorbed in this "dead layer" do not contribute to the diode's signal. Ignoring this layer is justified for a preliminary study, since Si is less absorbing than the SiO_2 over the range of wavelengths in my study. In addition, this hand-model can be expanded to include the layer later if necessary.
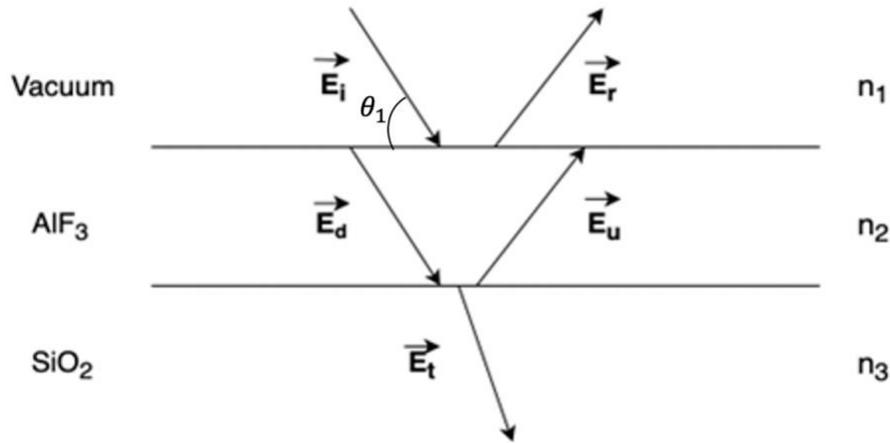
Fig. 6.   The multilayer interface of aluminum fluoride and silicon dioxide to calculate the transmission. The subscript "d" to signal the downward electric field and the subscript "u" is to signal the upward electric field in the layer. Source: Made using Diagram Editor [22].

2.4.1 Fresnel Coefficients

The next step in rigorously modeling the data is to use Fresnel coefficients. Based on the diagram we can also compute transmission into the silicon detector using Fresnel coefficient optics as shown in many standard optics texts. However, since I use grazing angle instead of angles measured from normal, I had to rewrite the equations, switching sine functions [23, eq. (4.1), (4.2), (4.3)]. As a ray with incident electric field (E_i in Fig. 6.) strikes the first layer a fraction transmits, the rest reflects. Fig. 6 is a useful schematic in showing each of the rays and the amplitudes of the components of the reflected and transmitted electric fields at the boundaries between layers.

Fresnel coefficients are the relationship between plane waves. Augustin Fresnel, who wrote the relationships, found the ratios of the transmitted and incident electric fields as well as the ratio of the reflected electric field and the incident field [23, p. 77].

Based on the calculations needed for the transmission through the SiO_2, there are four of the six Fresnel coefficients needed to calculate the transmission for this interface.

14

- $t_{12}, t_{23}, r_{21}, and\ r_{23}$

Where the subscripts t and r denote the transmission and reflection coefficients respectively, and the subscript shows which interfaces and which direction they are representing. For example, t_{12} is the transmission coefficient for light traveling from medium 1, the vacuum layer, to medium 2, the AlF$_3$. Medium 3 is the bottom layer, SiO$_2$. Since there are two types of polarization, there is notation to indicate this. The two types are s and p polarization. The s-polarization is the component of the electric field perpendicular to the plane of incidence. The "s" stands for *senkrecht* which means perpendicular in German [23, p. 74]. The p-polarization, "p" for parallel, is the electric field component that is parallel to the plane of incidence.

$$t_{12}^{(s)} = \frac{2 \sin \theta_1}{\sin \theta_1 + n_2 \sin \theta_2} \tag{5}$$

$$t_{23}^{(s)} = \frac{2 n_2 \sin \theta_2}{n_2 \sin \theta_2 + n_3 \sin \theta_3} \tag{6}$$

$$r_{21}^{(s)} = \frac{n_2 \sin \theta_2 - n_1 \sin \theta_1}{n_2 \sin \theta_2 + n_1 \sin \theta_1} \tag{7}$$

$$r_{23}^{(s)} = \frac{n_2 \sin \theta_2 - n_3 \sin \theta_3}{n_2 \sin \theta_2 + n_3 \sin \theta_3} \tag{8}$$

and for p polarization we have similar equations.

$$t_{12}^{(p)} = \frac{2 \sin \theta_1}{\sin \theta_2 + n_2 \sin \theta_1} \tag{9}$$

$$t_{23}^{(p)} = \frac{2 n_2 \sin \theta_2}{n_2 \sin \theta_3 + n_3 \sin \theta_2} \tag{10}$$

$$r_{21}^{(p)} = \frac{n_2 \sin \theta_1 - n_1 \sin \theta_2}{n_2 \sin \theta_1 + n_1 \sin \theta_2} \tag{11}$$

$$r_{23}^{(p)} = \frac{n_2 \sin\theta_3 - n_3 \sin\theta_2}{n_2 \sin\theta_3 + n_3 \sin\theta_2} \tag{12}$$

With the definitions of these coefficients, the propagation of light can be calculated through the multilayer interface. These equations can be compared to equations found in literature, recalling that, since the angle used is measured from grazing, cosines are switched with sine [23, p. 78]

Another important relation is Snell's law for grazing angle which is

$$n_1 \cos\theta_1 = n_2 \cos\theta_2 \tag{13}$$

The well-known Pythagorean trigonometric identity, Equation (14), allows one to create Equation (15) below.

$$\sin^2\theta + \cos^2\theta = 1$$

$$\sin\theta = \sqrt{1 - \cos^2\theta}$$

By combining Snell's Law, Equation (13), Equation (15), the Pythagorean identity, and noting that $n_1 = 1$ is the index of refraction of vacuum, we obtain

$$n_2 \sin\theta_2 = n_2\sqrt{1 - \cos^2\theta_2} \tag{16}$$

Further simplifying and substitution of angles with Snell's Law we get equation 17,

$$\sin\theta_2 = \sqrt{1 - \frac{\cos^2\theta_2}{n_2^2}} \tag{17}$$

By defining the reflection and transmission coefficients as $\alpha_{12} = \frac{\sin\theta_2}{\sin\theta_1}$ and $\beta_{12} = \frac{n_2}{n_1}$ we can calculate the following relations.

By using Equation (17) for $\sin\theta_2$ and $n_1 = 1$ we can show

$$\alpha_{12} = \frac{\sqrt{1 - (\cos\theta_1/n_2)^2}}{\sin\theta_1} \tag{18}$$

$$\beta_{12} = n_2 \tag{19}$$

There are analogous equations for each of the subsequent interfaces, from interface 2 to 1 and 2 to 3, and so on.

Then using Equations (18) and (19) combined with the equations of Fresnel coefficients- Equations (5) through (12)- we can write for s polarization:

$$t_{12}^{(s)} = \frac{2}{1 + \alpha_{12}\beta_{12}} \tag{20}$$

$$r_{21}^{(s)} = \frac{1 - \alpha_{21}\beta_{21}}{1 + \alpha_{21}\beta_{21}} \tag{21}$$

$$t_{23}^{(s)} = \frac{2}{1 + \alpha_{23}\beta_{23}} \tag{22}$$

$$r_{23}^{(s)} = \frac{1 - \alpha_{23}\beta_{23}}{1 + \alpha_{23}\beta_{23}} \tag{23}$$

And for p polarization:

$$t_{12}^{(p)} = \frac{2}{\alpha_{12} + \beta_{12}} \tag{24}$$

$$r_{21}^{(p)} = \frac{\alpha_{21} - \beta_{21}}{\alpha_{21} + \beta_{21}} \tag{25}$$

$$t_{23}^{(p)} = \frac{2}{\alpha_{23} + \beta_{23}} \tag{26}$$

$$r_{23}^{(p)} = \frac{\alpha_{23} - \beta_{23}}{\alpha_{23} + \beta_{23}} \tag{27}$$

2.4.2 Propagation Constant

The propagation constant, C, which I will now discuss, measures the change of the amplitude and phase of an electric field propagating from one medium to the next [24]. It is a complex quantity with both imaginary and real components. The attenuation constant is the name given to the real part of the propagation constant. It causes a decrease in amplitude of the electric field.

To calculate the transmission of an electromagnetic wave electric field propagating from layer to layer we must calculate the phase shift in the oscillating electric field in each layer of the multilayer film. This propagation accounts for the shift created in it due to traveling through a specified thickness of each layer. The amplitude of the electric field changes according to e^{ikz} where z is the thickness of the film and k is the wave number [23, pp. 94-95]. It is important to note at this point that the wave number of a wave depends on the index of refraction of the media it is propagating through. $k = \frac{2\pi}{\lambda}$ so we can say

$$C = \exp(in_2 kd \sin \theta_2) \tag{28}$$

Putting Equation (13) and Equation (17) into Equation (28) can be written as

$$C = \exp \frac{2\pi id}{\lambda} \sqrt{n_2^2 - \cos^2 \theta_1} \tag{29}$$

Where C is the propagation constant and n_2 is the complex index of refraction of material 2, the AlF$_3$ layer.

2.4.3 Electric Field Calculations

Based on the convention that the initial electric field is at the intersection between two layers and the amplitude and phase changes as the light goes through the layer, the transmission through the layers can be shown to be.

$$E_t^{(s)} = C E_d t_{23}^{(s)} \tag{30}$$

$$E_d^{(s)} = E_i t_{12}^{(s)} + C E_u r_{21}^{(s)} \tag{31}$$

$$E_u^{(s)} = C E_d r_{23}^{(s)} \tag{32}$$

These formulas are derived by the geometry of the multilayer interface with the assumption the "original" electric field refers to the top surface of the layer, and its amplitude and phase changes as it passes through the layer. As the wave goes through the middle medium, the phase is multiplied by the propagation constant, C. For E_d, where the subscript "d" stands for the downward component of the electric field, we have the component of the initial electric field, E_i, as it is transmitted through the first interface intersection, so it is multiplied by the transmission coefficient of medium 1 to the second medium. The other component is the reflection of the electric field label E_u, where the subscript "u" is to signify the upward component of the electric field, but by the time it reflects with the vacuum layer it has been shifted by the propagation constant, so it is multiplied by C, to get the total, we add those two components together.

2.4.4 Reflectance and Transmission

With all these derivations of the Fresnel coefficients, and the electric fields and the definition of a few other terms, the final transmission through an interface was through a multilayer interface. For the bottom layer of the interface, there is reflectance, R_{23}, which is the reflectance of between medium 2 to medium 3. By definition

$$R_{23} = |r_{23}|^2 = \left| \frac{E_u}{C E_d} \right|^2 \tag{33}$$

Replacing r_{23} in Equation (33) with Equation (23) we obtain

$$R_{23}^{(s)} = \left| \frac{1 - \alpha_{23}\beta_{23}}{1 + \alpha_{23}\beta_{23}} \right|^2 \tag{34}$$

The complex math and simplification is shown, where the * represents the conjugate since

$\alpha \; and \; \beta$ coefficients are complex.

$$R_{23}^{(s)} = \frac{(1 - \alpha_{23}\beta_{23})(1 - \alpha_{23}^*\beta_{23}^*)}{(1 + \alpha_{23}\beta_{23})(1 + \alpha_{23}^*\beta_{23}^*)} \tag{35}$$

$$= \frac{1 + |\alpha_{23}|^2|\beta_{23}|^2 - 2\Re(\alpha_{23}\beta_{23})}{1 + |\alpha_{23}|^2|\beta_{23}|^2 + 2\Re(\alpha_{23}\beta_{23})} \tag{36}$$

And then we have T_{23}, the transmission between the second and third medium for both s and p

polarization.

$$T_{23} = 1 - R_{23} \tag{37}$$

Further discussion on Equation (37) is developed on this in section 3.6 and 3.8 of this paper.

By continuing the simplification, it follows

$$T_{23}^{(s)} = 1 - R_{23}^{(s)} \tag{38}$$

$$T_{23}^{(s)} = 1 - \frac{1 + |\alpha_{23}|^2|\beta_{23}|^2 - 2\Re(\alpha_{23}\beta_{23})}{1 + |\alpha_{23}|^2|\beta_{23}|^2 + 2\Re(\alpha_{23}\beta_{23})} \tag{39}$$

$$= \frac{4\Re(\alpha_{23}\beta_{23})}{1 + |\alpha_{23}|^2|\beta_{23}|^2 + 2\Re(\alpha_{23}\beta_{23})} \tag{40}$$

The final simplification ends with

$$T_{23}^{(s)} = \Re(\alpha_{23}\beta_{23})\left| t_{23}^{(s)} \right|^2 \tag{41}$$

And thus, we can say the final transmittance of plane waves passing through the entire interface

is

$$T^{(s)} = \Re(\alpha_{23}\beta_{23})\left| E_t^{(s)} \right|^2 \tag{42}$$

$$= \mathrm{R}(\alpha_{23}\beta_{23}) \left| \frac{Ct_{12}^{(s)}t_{23}^{(s)}}{1 - C^2 r_{21}^{(s)} r_{23}^{(s)}} \right|^2 \tag{43}$$

And similar simplification done from Equation (38) to (43) is done with the corresponding p-polarized equations is omitted in this paper but the outcome is

$$T_{23}^{(p)} = \Re(\alpha_{23}\beta_{23}^*) \left| t_{23}^{(p)} \right|^2 \tag{44}$$

Finally, the total transmission through the entire multilayered interface for p-polarized light ends with

$$T^{(p)} = \mathrm{R}(\alpha_{23}\beta_{23}^*) \left| E_t^{(p)} \right|^2 \tag{45}$$

$$= \Re(\alpha_{23})\Re(\beta_{23}) \left| \frac{Ct_{12}^{(p)}t_{23}^{(p)}}{1 - C^2 r_{21}^{(p)} r_{23}^{(p)}} \right|^2 \tag{46}$$

Equations (25) and (27) are the final product of the derivation of equations. The transmission at different wavelengths was modeled with these equations to compare to the actual data taken at ALS.

2.5 Modeling the Bare Silicon Diode

After the models were compared to the actual data from previous models, it was found necessary to create a model to represent light going through bare silicon diode which is used to normalize the data before adding the effects of the AlF3. The method of normalization will be discussed in a later section.

2.5.1 Three-Component Model of Diode

The first model that was used to check if the transmission calculated by the electric field passing through a layer of SiO_2 matched the data sufficiently.

The modeling of the data was necessary for this process so the data could be normalized. Since the bare diode would read the maximum amount of the electric field, having this baseline would be able to lead to looking at the changes when the extreme ultraviolet waves passed through the AlF$_3$. Since silicon oxidizes, this model has vacuum as the top component, a layer of SiO$_2$, and the bottom is silicon. Normalization is by taking a reference of what the maximum transmission would be and then taking the readings of the photodiode and using that reference to show the transmission on a scale of 0 to 100% of the light that is transmitted.

2.5.2 A Four-Component Model of the Uncoated Silicon Diode

To get a more accurate model than modeling the diode with three components, another model was created with four components. This model employs two distances that can be fit but also includes another propagation constant due to the light transmitting through another layer. For the case of the bare silicon diode, the top is vacuum, then a layer of silicon diode, then dead layer of silicon, and lastly, an active layer of silicon as shown is Fig. 7.

By accounting for both a dead and active layer of silicon, there are additional reflection and absorption effects that change the total transmission through the uncoated diode. An approximation of the transmission through the dead layer was made using the Beer-Lambert Law. The new propagation constant through the third layer can be approximated as shown in Equation (22).

$$C_2 = \exp\left(\frac{2\pi i d_2 n_3 \sin\theta_3}{\lambda}\right) \tag{47}$$

As Fig. 7 shows, d_2 is the thickness of the third layer of the thin film, the dead layer of Si. θ_3 is the angle from grazing after the electric field enters the third layer and is refracted.

By using equation 22 as well as equations 13, 14, and 15 we can write the calculation for transmission through all the layers. This equation comes to be

$$T^{(s)} = 2I_0 |C_2|^2 R(\alpha_{23}\beta_{23})|E_t|^2 \tag{48}$$

$$T^{(p)} = 2I_0 |C_2|^2 R(\alpha_{23}\beta_{23}^*)|E_t|^2 \tag{49}$$

23

Here E_t comes from equation 13 and includes the first propagation constant and thickness for the

SiO$_2$ layer.

From Equations (29) and (30), both the index of refraction as well as the thickness of the layer

can be calculated. The parameters taken in for this fitting were the imaginary and real parts of the

index of refraction, along with the range of angles being studied. We used as initial guesses for

the index of refractions calculated using the webtool at the CXRO website. The density for the

amorphous SiO2 that grows on Si from thermal oxidation is known to be denser than fused

quartz. We used the density of the fused silica for early studies and the density of the grown

material for later work. Both worked well as starting places.

Chapter 3: Results and Discussion

In this chapter I will discuss the results found from the various models and the optical properties extracted.

3.1 Normalization of the Data

Normalizing the XUV diode's transmission data requires careful consideration. Reflectance data is normalized to the response of the reflectometer photodiode (# 3 in Fig. 5) at each wavelength in a way that cannot be duplicated for the XUV diode transmission data. The photodiode that measures the beam's straight-through intensity, I_0, is the same one which measures reflectance. To calculate a sample's reflectance at each angle or wavelength one divides photodiode #3's signal by I_0 after taking into account dark current. However, the XUV diode doesn't have such an I_0. What the XUV diode records is proportional to the intensity transmitted through the various optical layers and absorbed in the active portion of the photodiode. That absorption is smallest at 90°, but it is never zero. To have the transmission data normalized in a way for better analysis and application, it was necessary to guess at an I_0 to provide a first approximation for the normalization. Figures 8 and 9 show representative "raw transmission" data. That is, XUV diode output taken before normalization was attempted.

25
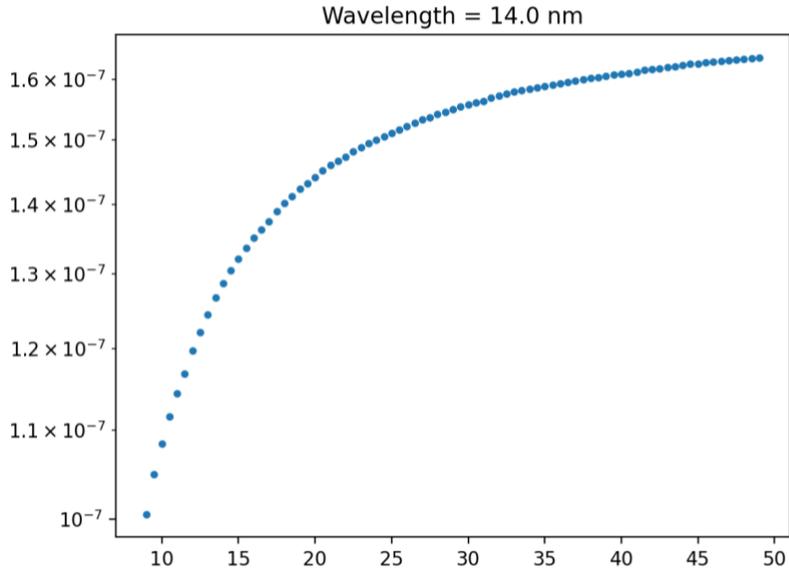
Fig. 8.   Uncoated (just the silicon diode), raw data of transmission at 14nm
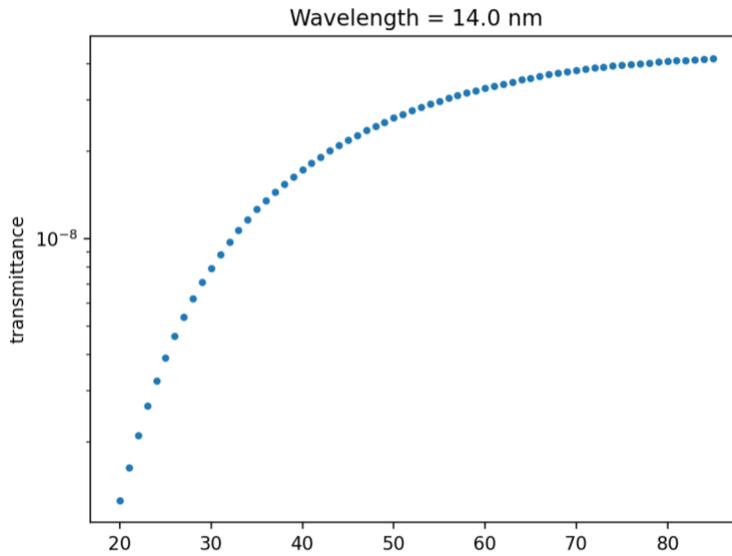
Fig. 9.   Raw Data of coated diode with AlF3 at 14 nm wavelength

In contrast with a lack of I_0 data, the "dark current," or the signal the diode produces when there is no light passing through the diode was easily obtained and dark current readings were taken often throughout the eight hours of measurement. The dark current was subtracted from the raw data before normalization.

26

Measurements of transmission and reflectance were taken over a wide range of wavelengths at ALS. At many of these wavelengths, there were measurements both of the bare diode and the coated diode, that is, the diode with the AlF₃ coating on top. The measurements taken through the bare diode gave the "maximum" signal since the AlF3 film would necessarily absorb some light. Indeed, Fig. 8 and 9, show that the uncoated diode saw more light than the coated diode. This true at all wavelengths.

3.1.1 Beer-Lambert Model Normalization

Using the reasoning that the uncoated diode data is the maximum transmission, is what enabled the normalization for the Beer-Lambert approximation. Using Equation (2), a model was created to fit the uncoated data at each corresponding wavelength. It fits the parameters κt and I_0 and, thus, can be used as a normalization factor for the coated data. By using the I_0 found through this method, Python's curve fit function was used to fit to the AlF₃ coated data.
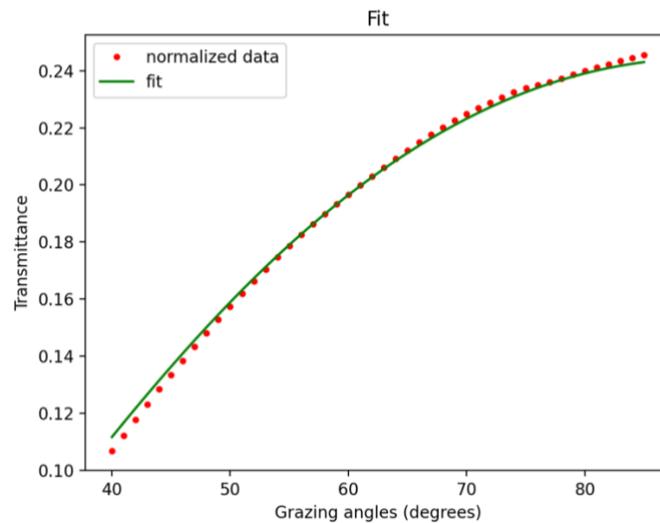
Fig. 10.   Fit of the coated AlF3 data at 14nm using Beer's Law Approximation. This represents a transmission percentage

Since we know the wavelength, and angle and what the imaginary part of the index of refraction is, the thickness can be extracted by dividing $2\kappa t$ by $2Im(n)$ based on Equation (4). This

method was used in order to extract the thickness of AlF$_3$ based on the Beer-Lambert Approximation.

3.1.2 Fresnel Calculations

One normalization procedure for the diode is to divide each value in a data set by the value of the last point. The last point was taken at near-normal incidence (90 degrees). It has the data set's highest transmission value. This procedure gives it the value of 1.0 (see Fig. 11.) *Thus, the "transmittance" shown on most graphs in this paper is not transmission percentage, but transmission relative to the transmission at 90 degrees.* An example is shown in Fig. 11.

Another method to normalizing the transmission percentage was to use the Beer-Lambert approximation to calculate a factor to scale the transmission to the approximate value of the initial light that reaches the active layer of the diode. Using Beer's Law Equations (3) and (4) the factor the diode's signal is multiplied by is

$$e^{-\frac{k_1 t_1}{\sin \theta} - \frac{k_2 t_2}{\sin \theta}} \tag{50}$$

Using this factor, a better normalization is found. Look at Fig. 11a and 11b to see the difference between the normalizations.
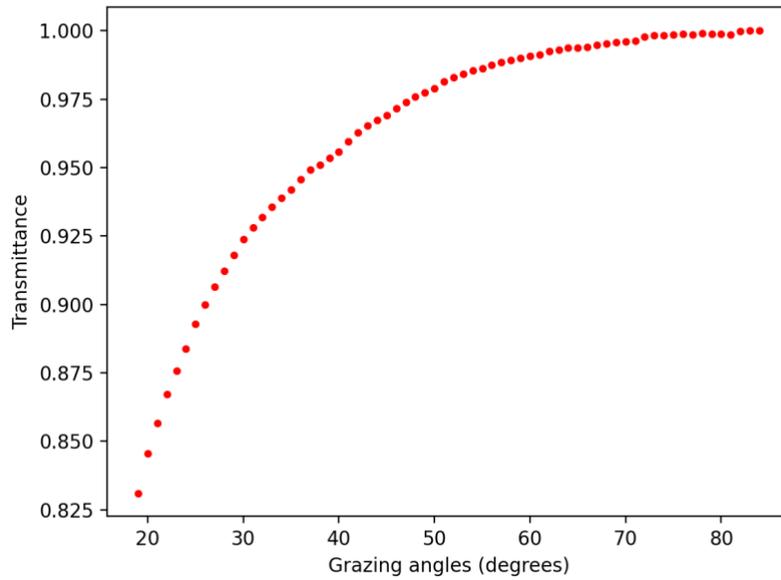
Fig. 11a.   Normalized data of the transmission at 15 nm for the bare silicon diode. This was normalized by taking the last measurement at about 90 degrees as the maximum transmission and dividing each reading by that number. That is why the last point is read as 1 on the graph.
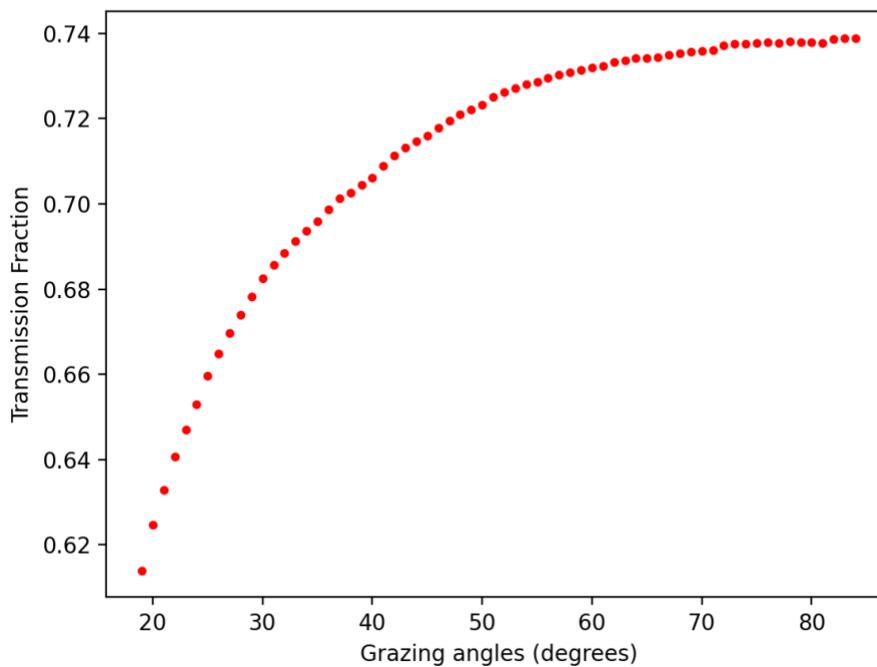
Fig. 11b.   The data plotted in Fig. 11 is multiplied by the absorption factor calculated using Beer's Law. This provides an estimate of the fraction of incident EUV light reaching the diode's active layer.

3.2 Beer-Lambert Law Fitting of Thickness

Having obtained the initial fitting using the Beer-Lambert Law approximation, the thickness of AlF_3 could be estimated.

However, since this approach did not consider the effect of the front-surface reflection from the multilayer, the reflection data were examined to determine the range for which the approximation is justified. As the angle advances from grazing, the reflection falls below 10% at 20°. It falls another 2.5 orders of magnitude by 38° and appears insignificant beyond 40° as show in Fig. 7. At angles larger than 38° the reflection is minimal and does not create major issues in the Beer-Lambert approximation. To not have contradictions in the model, which does not account for high reflectance, the data below 40 degrees was not used in the fitting of for $2\kappa t$ and I_0, using the Beer-Lambert Law.
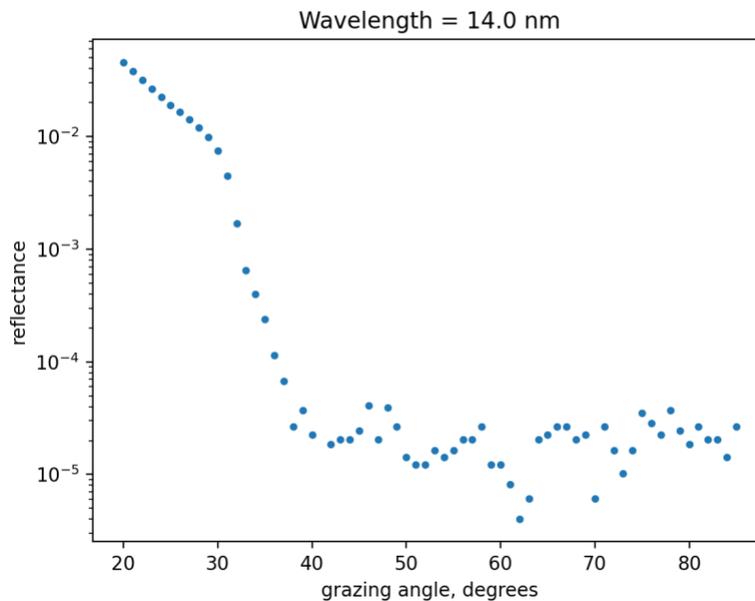
Fig. 12.   Raw reflection data from the ALS at 14 nm

30
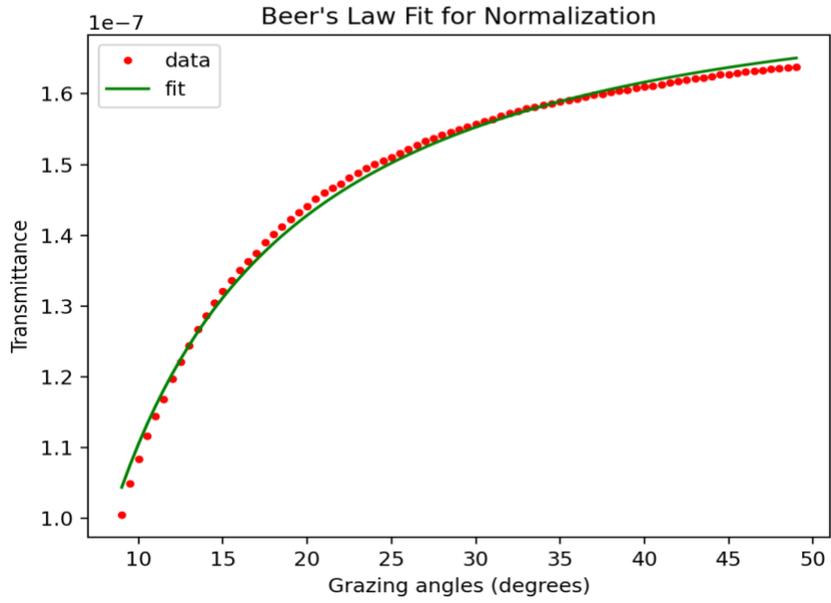
Fig. 13.   Unnormalized transmittance at 14 nm of the bare diode as modeled by Beer's Law. This fit is used as normalizing factor for the data with the aluminum fluoride thin film coating on top of the diode

Fig. 14. uses a ratio between the readings of the AlF_3 coated side with the signal from the bare

silicon diode. This way there this shows a percentage of the amount of light that passes through.
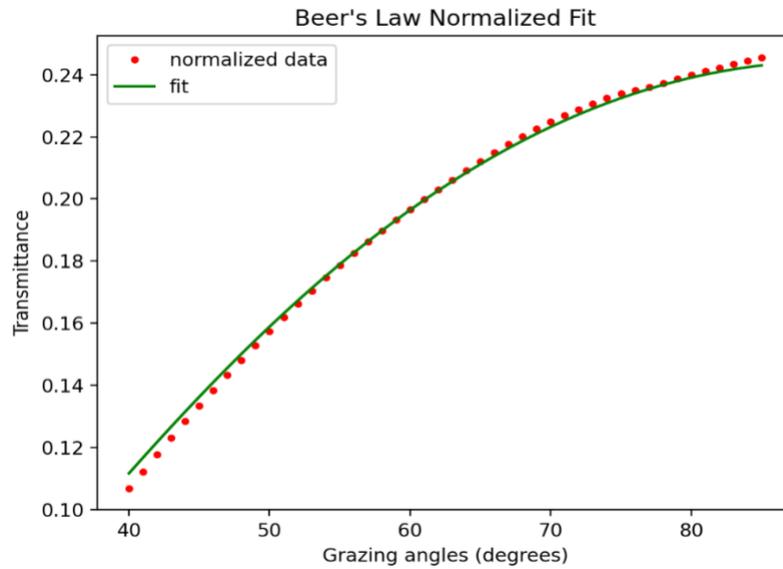
Fig. 14.   The normalized fit using Beer's Law for AlF_3 as well as the data of the 14 nm reading from ALS.

This model fits the angular dependent data for wavelengths where data on uncoated diode and the coated diode were available.
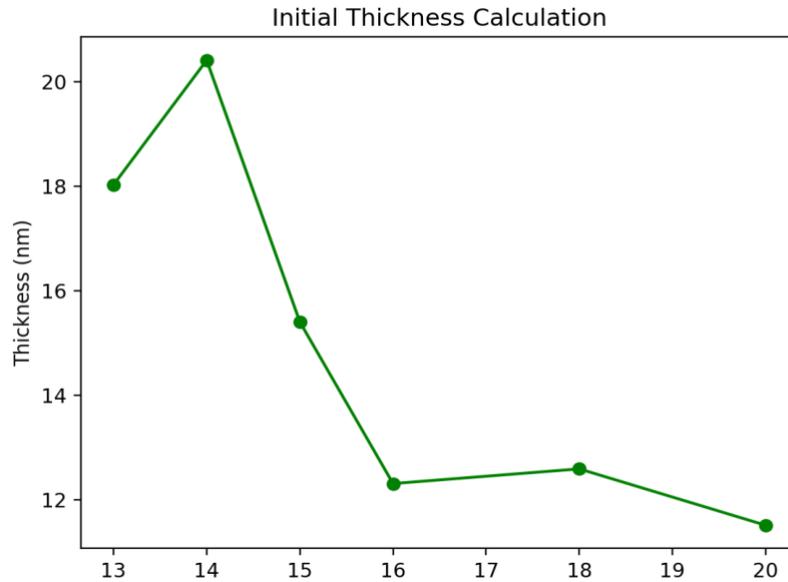
Fig. 15.   The plot shows the *apparent thicknesses* of the AlF_3 layer as found using the Beer's Law model using the literature values of indices of refraction. The thickness was extracted by using on Beer's Law. Of course, there is only one true thickness to be determined.

The uncertainties from the calculated thicknesses are quite small compared to the range of thicknesses and same for graphical purposes the error bars do not appear when plotted.

The figure invites several observations. First, the apparent thicknesses decrease with increasing wavelength. That is, for the shorter wavelengths the calculated thickness is significantly larger than the ones for longer wavelengths. From additional calculations (not shown) the trend is seen to continue out to the limit of measurements, 50 nm. These calculations of the AlF_3 thickness are based on literatures values for imaginary part of the index of refraction. Since the thickness of the aluminum fluoride thin film is constant, this inconstancy indicates that there could be an issue in the literature derived values of the imaginary part of the index of refraction for longer wavelengths.

This preliminary approximation seemed successful because it corroborated within a factor of 2 the estimated thickness of AlF$_3$ of 30 nm as estimated by those who took the measurements at the ALS.

3.3 Three-Component Fresnel Coefficients of Bare Diode

The first attempt at using the Fresnel coefficients was model the diode coated a layer of SiO$_2$. When transmission calculated (blue line in Fig. 16) from model was overlayed on the actual data, it is clear that the three-component model was not sufficient to model that data.
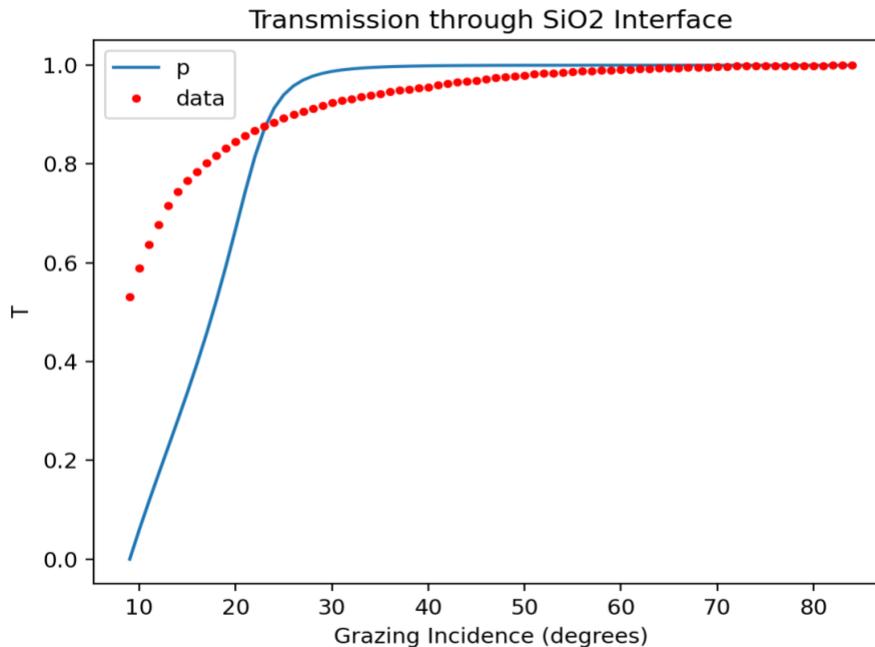
Fig. 16.   The p polarization as calculated by a-SiO2 on Si   (two-layer) model overlaid on top of the data taken at 15 nm. The dead layer is not taken into account in this model.   The deviation at grazing angles between 20 to 50 may be due to neglecting this layer.

The fit at near normal incidence is good but diverges quickly at lower angles. The computed transmission shows a steep fall below 30°—probably associated with total external reflection. Thus, we concluded that this model is inadequate. A better model needs to include the effects of the dead layer of silicon to be a more accurately match to the data.

3.4 Comparison Between Three-Component Fresnel Calculation and Beer-Lambert Law

After the model with the Fresnel coefficients and the propagation constant was calculated, it was compared against the Beer-Lambert law that was used in the previous fits. I observed that the calculated transmission of s and p polarized light using Fresnel coefficients is close to the Beer-Lambert Law approximation at 15 nm and lower. I noted that at the shorter wavelengths the transmission of s and p polarized light are almost indistinguishable. However, as the wavelengths got longer s and p polarization began to differ more and more.
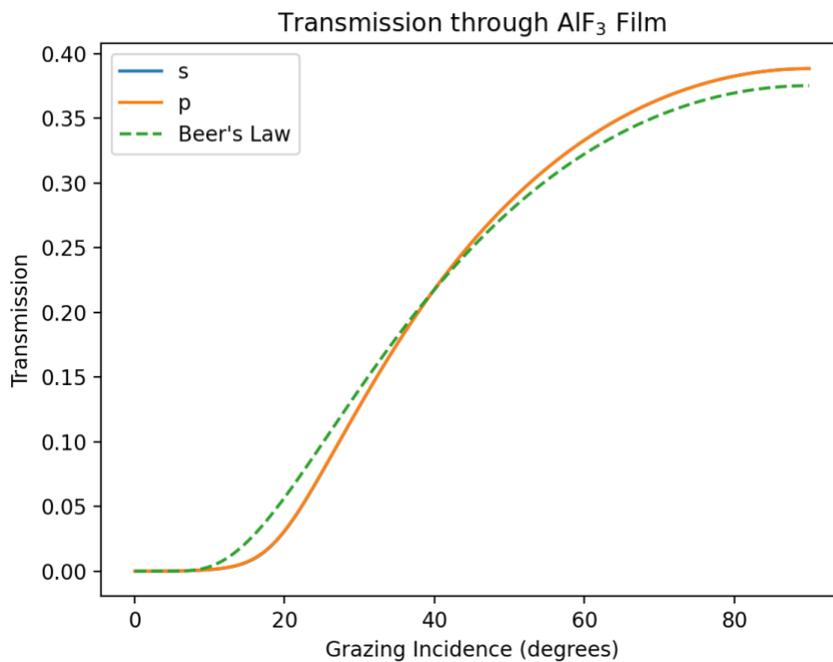
Fig. 17.   Comparison of s and p polarization as well as the approximation made with the Beer-Lambert law at 15nm wavelength

As shown in Fig. 17., we can see that there are some slight differences in these models. Because of this apparent difference in the models led to the shift in which modeled we used (using Fresnel coefficients instead of Beer's Law).

In summary, we used the Beer-Lambert model as a preliminary fit to the thickness of the AlF$_3$ but decided we needed to develop other procedures based on the Fresnel coefficients to better fit the data.

3.5 Fits of Four-Component Model of Diode

The three-component model was not sufficient in modeling the data from ALS as the overlaid plots show (Fig. 16.). To improve the model, a four-component model of the bare silicon diode was made to describe the layers more accurately in the diode. This model included both the dead and active silicon regions below the SiO$_2$ overlayer as described in the methods chapter.

When the model was used over the entire range of angles, the fit was very bad, but when the lower angles were omitted, the model matched the data very well. An example of a fit using data above 19 degrees is shown in Fig. 18.
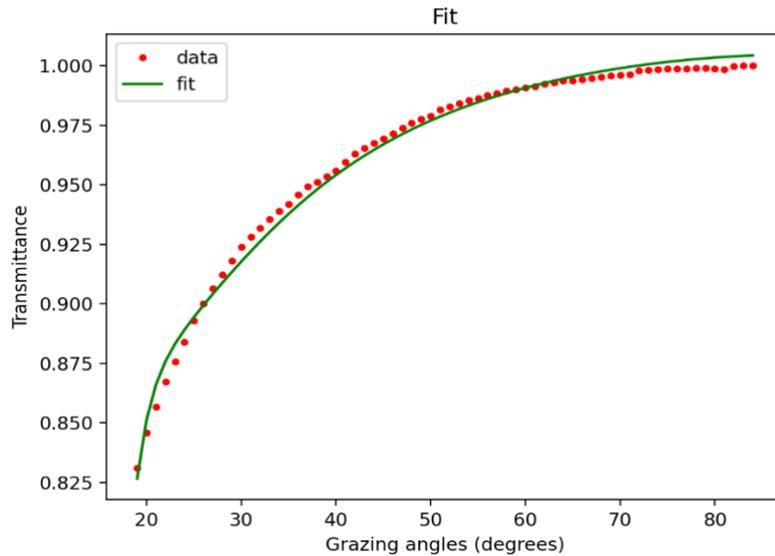
Fig. 18.   Transmission of 13 nm light into the active layer of the diode was used to compute thicknesses of SiO$_2$ and dead layer. Fitting the thickness using the four-component model of the bare diode.

This model fit the data very well across the wavelength, but only when the low angle was excluded. Experience showed that it was important to pick the proper cut off angle. There was a function using Python programming language to omit specified angles. There was a threshold angle where the fit was best. I was able to find that angle because when the omitted data was increased to include even one degree more, the fit broke down. I judged with trial and error the best fit where the fit matched the data very closely and where the thickness fit was a maximum. There was a certain angle where the angle found to be the best would decrease in both directions.

3.5.1 Total External Reflection

Table 1.   Angles that were used for the best (maximum) fit of the thickness using the four-component model

Wavelength	Cut off Angle for Fit	Critical angle for Total External using Literature Values
12.5 nm	15°	9.9°
13 nm	16°	11.3°
14 nm	18°	12.8°
15 nm	19°	14.0°
17.1 nm	25°	16.2°
20 nm	30°	18.6°
21 nm	15°	19.6°
25 nm	40°	22.3°
25.6 nm	41°	22.6°
30 nm	50°	24.8°
30.4 nm	48°	25.0°
34	-	26.1°
42.0	-	27.4°
49.5	-	42.47°

From Table 1, the cut-off angle can be seen to trend upward as the wavelength increases. When the wavelength is longer, the smaller angles deviate from the model more, and the best fit comes from confining the fit to angle above the angle specified in the chart.

This phenomenon found in Table 1 resembles total internal reflection. It occurs when a ray of light coming from vacuum with an index of refraction of 1 hits a medium with an index of refraction less than 1 [25]. In the XUV range, as in the x-ray range, the real part of the index of refraction is less than 1 and therefore total external reflection can occur at low angles. Total external reflection is calculated with Snell's Law, Equation (13). By using the real part of the index of refraction at a desired wavelength and index of vacuum we can find the angle where this occurs.

$$Critical\ Angle = \cos^{-1}\frac{\Re(n_2)}{n_1} \tag{51}$$

Total external reflection causes issues in the model because at this point the transmission decreases dramatically with decreasing angle. The fit accounts for this extremely fast decrease in the computed transmission seen in the figures. In contrast, the data shows high transmission at lower angles. Since the low-angle transmission at longer wavelengths is larger than what the model finds, I conclude that, based on low-angle transmission, the delta value that the model calculated may be larger than the data justified.

There obviously seems to be an outlier from the increasing trend of the cut-off angle at 21 nm data and that may be because of the conditions of the measurement taken at this wavelength. These measurements were taken through the night over a span of about 12 hours. The time can lead to differences in dark current measurements. The dark currents are the measurements that the photodiode picks up when there is no light in the photodiode. These different conditions could have led to outliers like the 21 nm measurement from this data set.
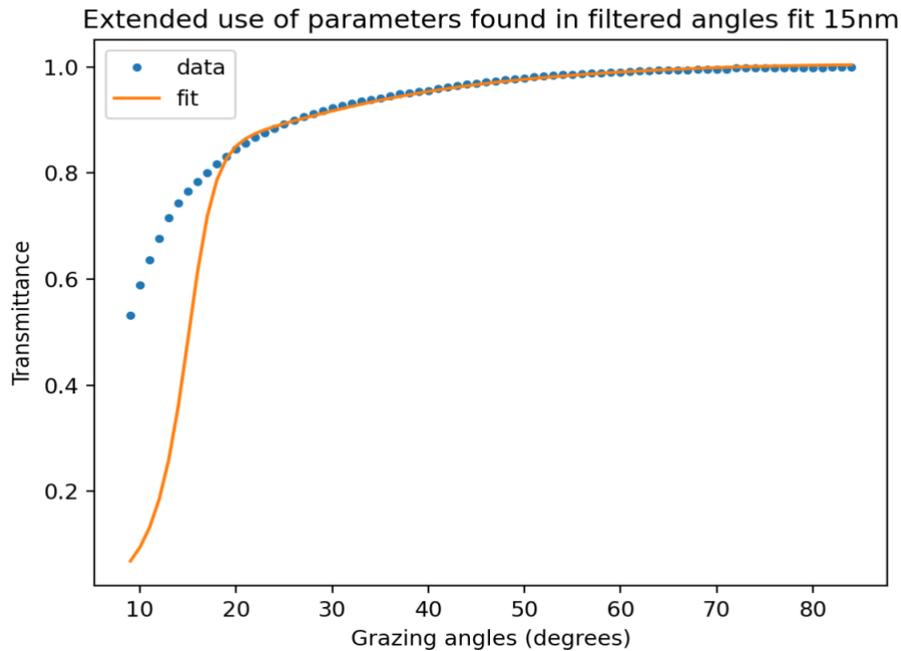
Fig. 19.   Using the fit thickness and other fit parameters, this is the overlay of that fit over the actual data.

After the thickness was fit, it and the optical constants were used to compute transmission and was overlaid on the data to see how well of a fit it was. The model fits very well from the cutoff angle (19°) to 90° but deviates drastically for angles shorter than 19° as shown in Fig. 19 and Table 1. The plot shows that there is dramatically higher transmission than what the computational model predicts. The transmittance of the data at 10° is more than five times greater than what the model predicts. It appears that more light enters the diode than what total external reflection should allow with these optical constants.

3.5.2 Thickness of SiO_2

It was now clear that before we could fit the accurately the thicknesses of the AlF_3 and its optical constants, it was necessary to fit the thickness of the layers in the silicon diode. After seeing that the model using Fresnel coefficients to model the diode as SiO_2 on Si, without the dead layer was insufficient, a model was developed that included all three layers: SiO_2, dead

layer of silicon, then lastly, the active layer of silicon. The next set thickness calculations also used a greater range of measurements and a wider range of wavelengths to get a better view of what was happening.

The results for the SiO_2 thicknesses found in using this model merit comment. As can be seen from Fig. 20, is that the error bars determined for the lower wavelengths are much smaller than those for the longer wavelengths. The error bars shown in Fig. 20 show that the model had some major inadequacies. Some of my previous studies that have shown the same trend in estimating the error bars derived for SiO_2 thicknesses when the indices are not allowed to vary much from starting values. An analogous pattern was seen in the fitting of Beer's Law (Fig. 15,) in that case, the best fit for longer wavelengths was with a smaller thickness, which I attributed to the issues in the literature values of the indices of refraction.
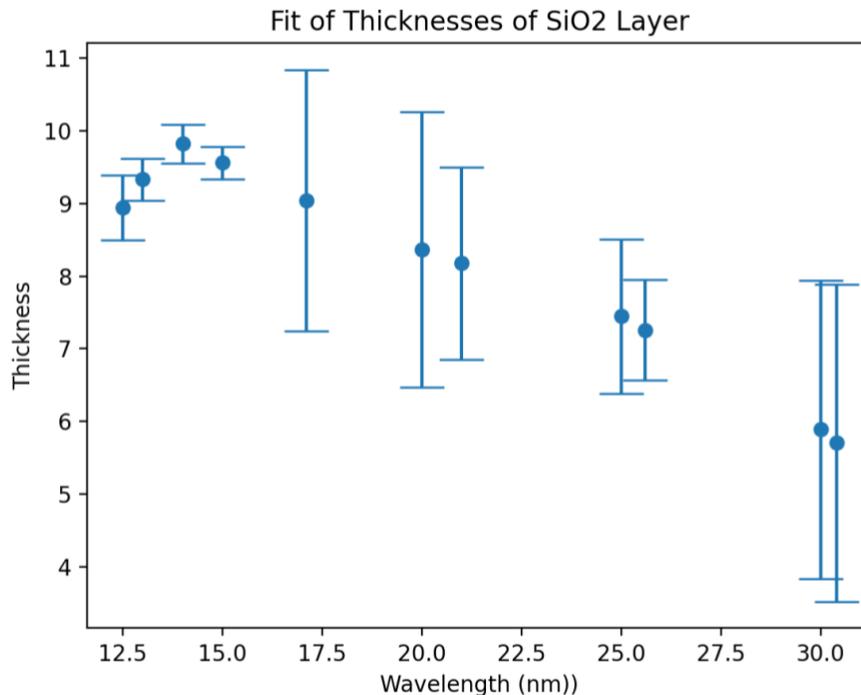
Fig. 20.   Thicknesses found for SiO_2 for a series of wavelengths.

Since the uncertainties were so large for wavelengths larger than 15 nm, I found the weighted average of just the first four wavelengths were found to be 9.474 nm. Then the weighted average of all the wavelengths brought down the thickness significantly. The average for all fit wavelength data is 8.927 nm.

Interestingly, the thickness of this third layer, the dead layer, came out to be 11.5 nm for almost all fits. Why there was not much deviance in this value across many wavelengths is unknown. Likely the indices of silicon are better known than SiO_2 and AlF_3.

3.5.3 Index of Refraction Fitting

In the previous sections, the index of refraction of AlF_3 and SiO_2 used in calculations were extracted from literature. I iteratively solved for the indices and thicknesses. Using the literature values as a starting point I found a thickness. I could then use it to fit for the index of refraction using the same four-component model After I found the two different numbers of the possible thicknesses of the layer; I used the two different thicknesses to fit both the real and imaginary parts of the index of refraction of SiO_2 at each wavelength.
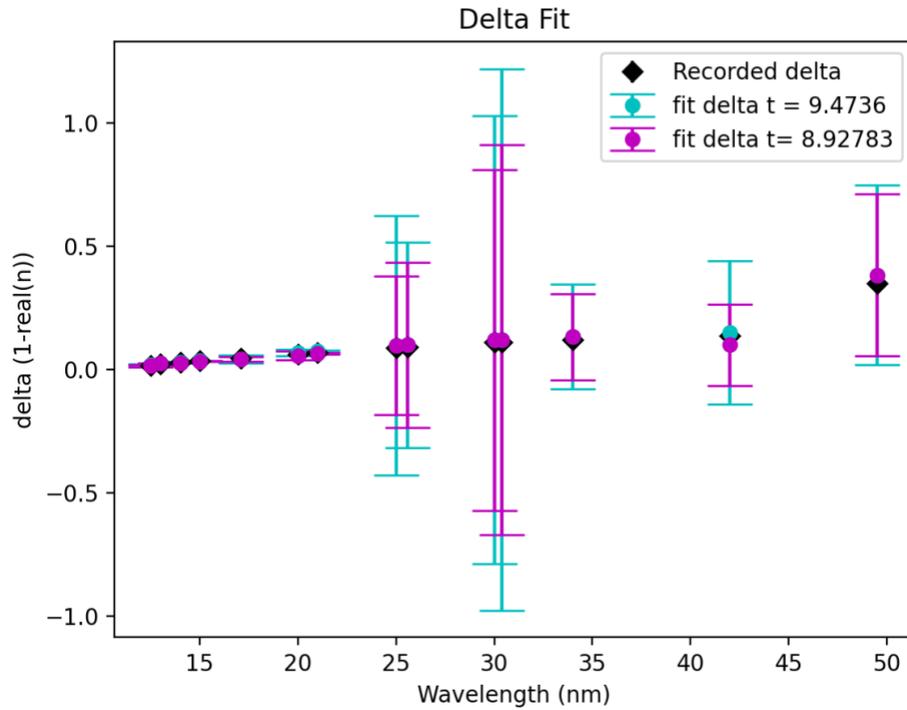
Fig. 21   This plot includes the values found in this study for each wavelength using both 9.4736 nm and 8.9783 nm for the SiO$_2$ layer (d$_1$ on Fig. 7) and both calculated values used 11.5 nm for the dead layer of Si (d$_2$ on Fig. 7). They are also plotted with literature values of SiO$_2$ from CXRO and Palik.

As shown in Fig. 21, we can see that the value of delta for two estimated thicknesses match that derived from the literature with very small error bars for wavelengths up to 21 nm. Then at the 25 nm wavelength the calculated uncertainties (error bars) grow much larger. This discrepancy in values corroborates the findings of other studies that the literature-derived indices for SiO$_2$ are not correct for grown-SiO$_2$ on a diode detector.
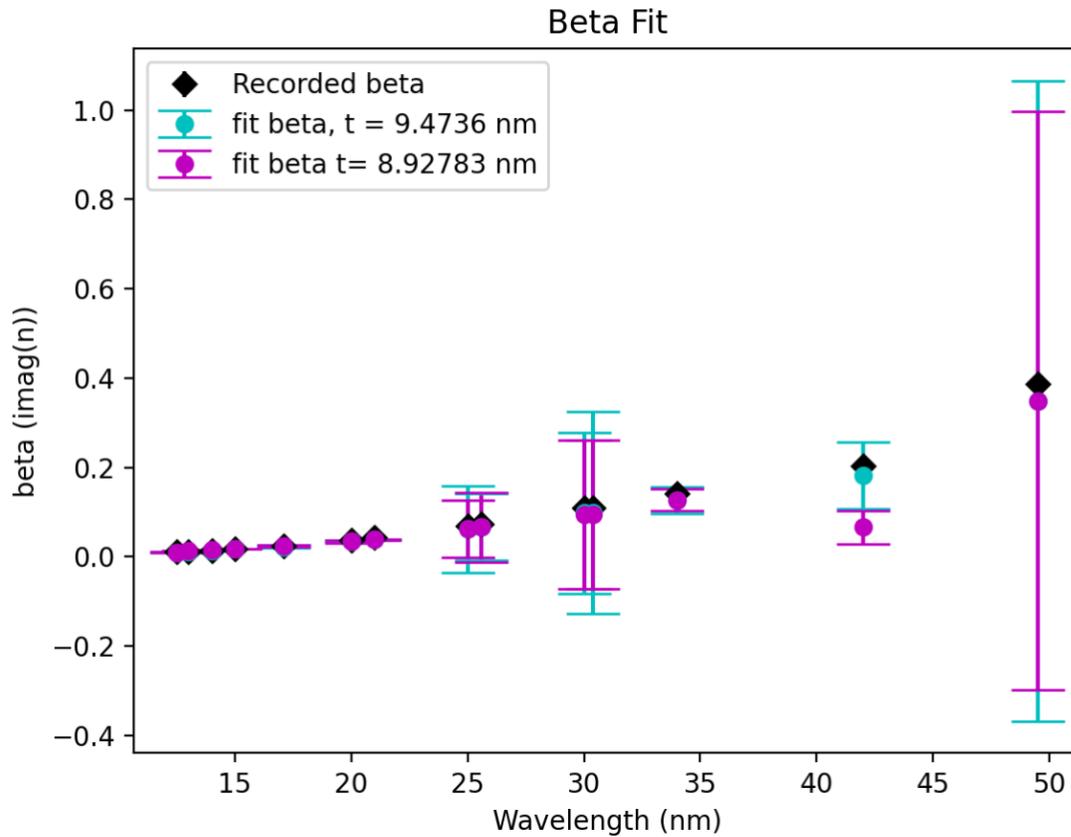
Fig. 22   The imaginary part of the index of refraction for SiO2 compared to the literature values. Look at Fig. 21 caption for information on the thicknesses used in the fits.

Since the findings of the thicknesses outputted two possible thicknesses that could be used in the fittings for index of refraction, I plotted the results of the indices of refraction that the model produced with the corresponding thicknesses. We have both the delta and beta fit as compared to the value of the index of refraction that I originally used to find the thickness. In this first case, I used the indices of refraction of fused silica from a combination of CXRO and Palik data. At first glance it looks like the values for both thicknesses are close to the literature derived values but uncertainty (error bars) and deviance from the literature derived value generally increases with wavelength.
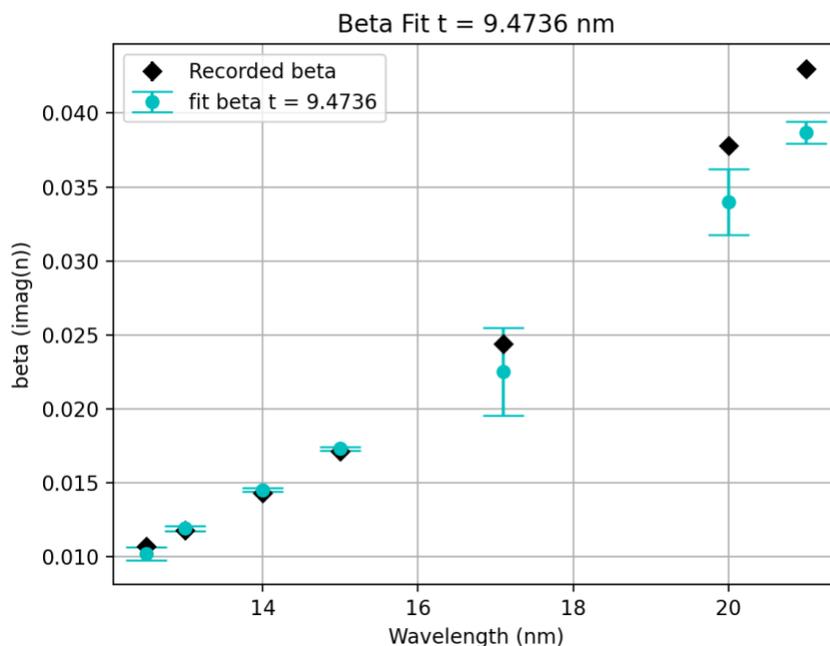
Fig. 23   This is the fit of the of the imaginary part (beta) of the index of refraction when the thickness was 9.47 nm in cyan and the literature values are plotted in black.
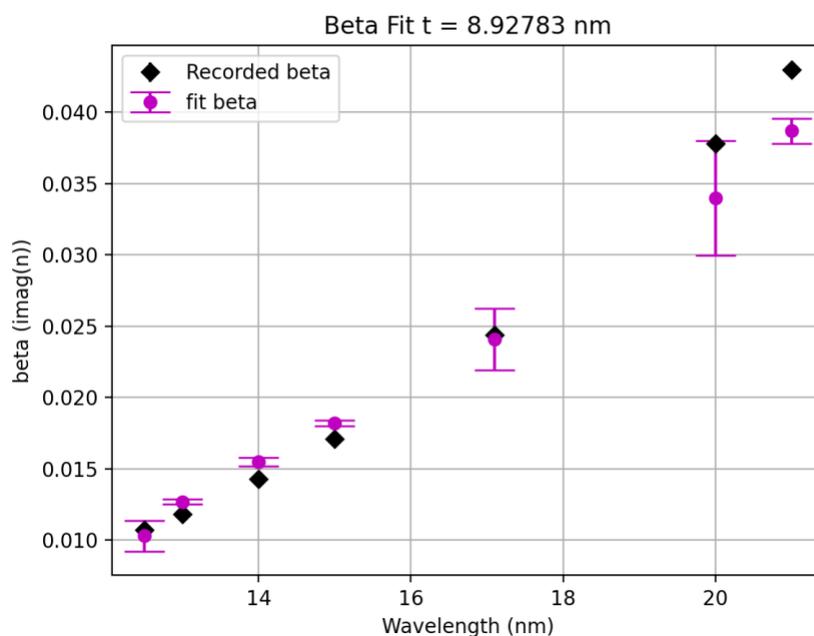
Fig. 24.   This is the same plot as Fig. 22, but just the SiO_2 thickness of 8.92783 nm was used with a closer view up to the 21 nm wavelength. It shows that there are discrepancies across all the wavelengths compared to the literature values of the index of refraction from CXRO.

Table 2 below includes the refractive indices from my work—also plotted in Fig. 23 and 24- along with literature values of amorphous silica. The values were generated from CXRO up to 41 nm while after 42 nm up to 49.5 nm are from a chapter in Palik volume 1.

Table 2.   This table includes the values found from the model for the index of refraction of the silica from the diode. The literature n and beta are from CXRO and Palik data. Note: the literature values from 15 nm to 34 nm were linearly interpolated from the values generated from CXRO.

λ (nm)	δ	1- δ = n	Literature n	Literature β	β
12.5	0.0192 ± 0.0028	0.9808	0.985121	0.009060	$0.0102 \pm 4.43e\text{-}4$
13	0.0254 ± 0.0012	0.9746	0.9803	0.01001657	$0.0119 \pm 1.73e\text{-}4$
14	0.0297 ± 0.0013	0.9703	0.9750	0.012109	$0.0145 \pm 1.27e\text{-}4$
15	0.0357 ± 0.0011	0.9643	0.970019	0.0145248	$0.0173 \pm 1.39e\text{-}4$
17.1	0.0414 ± 0.0157	0.9586	0.960458	0.02109301	$0.0225 \pm 2.98e\text{-}3$
20	0.0682 ± 0.0136	0.9318	0.947402	0.03207991	$0.0340 \pm 2.22e\text{-}3$
21	0.0742 ± 0.0049	0.9258	0.942745	0.0364795	$0.0387 \pm 7.39e\text{-}4$
25	0.0969 ± 0.5267	0.9031	0.925218	0.0584283	$0.0620 \pm 9.74e\text{-}2$
25.6	0.0995 ± 0.4169	0.9005	0.923203	0.06213357	$0.0668 \pm 7.41e\text{-}2$
30	0.1213 ± 0.9098	0.8787	0.907676	0.08977118	$0.0981 \pm 1.81e\text{-}1$
30.4	0.1213 ± 1.0988	0.8787	0.906379	0.09256699	$0.0981 \pm 2.26e\text{-}1$
34	0.1324 ± 0.2128	0.8676	0.897781	0.11970794	$0.127 \pm 2.95e\text{-}2$
42	$.1497 \pm 0.2910$	0.8503	0.8878	0.1672	$0.182 \pm 7.54e\text{-}2$
49.5	0.3839 ± 0.3653	0.6161	0.7376	0.3224	$0.349 \pm 7.17e\text{-}1$

It is important to note that in calculating the values in table 2 the models were constrained to not deviate more than ten percent above or below the preliminary index of refraction used. This raised issues as when the thickness of the SiO_2 layer was set to 9.47 nm. The model was not able to find a good fit to the data with these bounds. This is why the uncertainty for the longer wavelengths is so large.

In order to get a better fit, the data was fit again. this time the starting indices for SiO_2 were derived from amorphous silica using the density for grow oxide. More importantly I increased the bounds for the indices in the model to 30% for the shorter wavelengths up to 20

nm, and to 40% for the wavelengths longer than 20 nm. By increasing the bounds, the model was

able to find values for the index of refraction so the fit closely matched the data.

Table 3.   This table has the finals values of the indices of refraction found in this work for each wavelength. This extended the bounds so the fit values found by the curve fit model in python could deviate more from the literature values used as first values.

λ (nm)	n = 1 - δ	β
12.5	0.9899 ± .0054	0.00757 ± 1.28e-3
13	0.9866 ± 0.0056	0.00944 ± 1.40e-3
14	0.983 ± .0051	0.0125 ± 1.26e-3
15	0.9643 ± 0.0011	0.0173 ± 1.39e-4
17.1	0.9657 ± .0157	2.01e-2 ± 3.88e-3
20	0.9642 ± .0116	2.67e-2 ± 3.19e-3
21	0.9498 ± .0114	3.29e-2 ± 2.75e-3
25	0.9490 ± 0.0332	4.63e-2 ± 1.03e-2
25.6	0.9477 ± 0.0200	4.56e-2 ± 6.56e-3
30	0.9287 ± 0.0616	6.31e-2 ± 2.33e-2
30.4	0.9286 ± 0.0714	6.31e-2 ± 2.71e-2
34	0.9285 ± 0.0057	7.00e-2 ± 2.26e-3
42	0.9187 ± 0.0141	8.36e-2 ± 6.01e-3
49.5	0.8751 ± .0695	8.29e-2 ± 3.49e-2
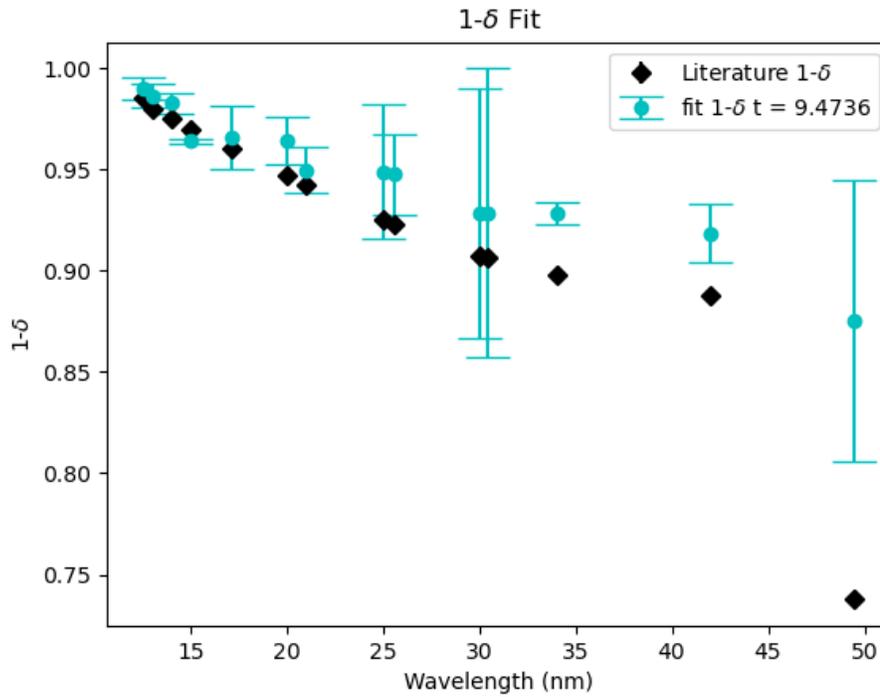
Fig. 25. Real part of the refractive index (n) values on Table 3. Value derived from literature sources are diamonds, while values obtained in this study are cyan circle with error bars. In this fitting the bounds for deviation from the literature values were in.
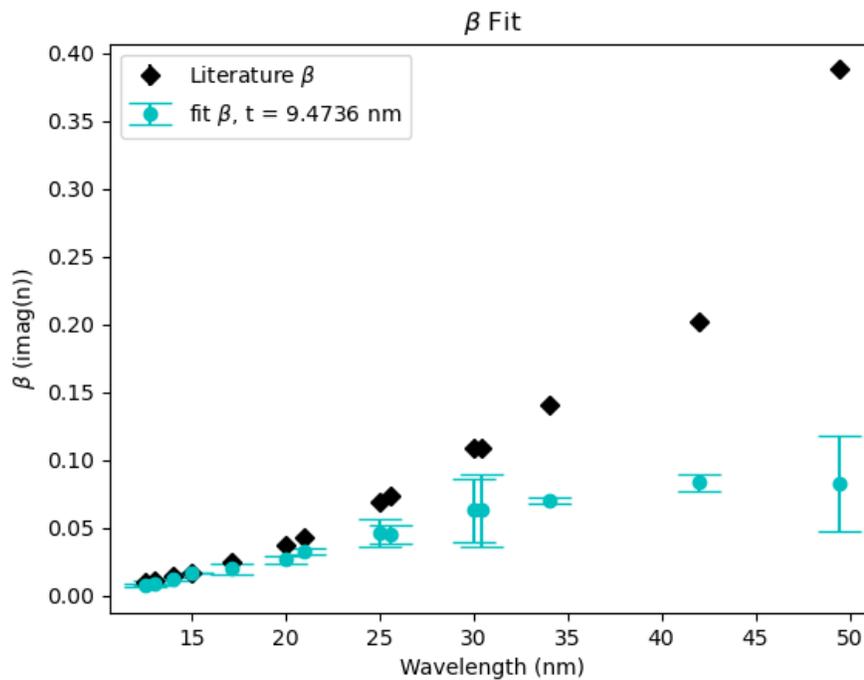

Fig. 26. β values from Table 3. Value derived from literature sources are diamonds, while values obtained in this study are cyan circle with error bars.

3.6 Additional Discussion

The values of the indices of refraction deviate from the values derived from literature as Fig. 25 and 26 show. The model that uses Fresnel coefficients to compute transmission with the literature indices shows the effect of total external reflection. At low angles the transmission is drastically lower than measured transmission as shown in Fig. 19. The data show that more light passes through the diode than the model will allow. Because of that major difference in the model from the data, the derived β values that were a significantly smaller than the literature β values from 20 to 49.5 nm.

The values of the indices of refraction found in this study corroborate with the findings of Zoe Hughes [26]. She also found through her methods that indices of refraction are very close to what the CXRO database records for shorter wavelengths, while her values deviate more from their values at the longer wavelengths. This could be due to the limitations of the Independent Atom Approximation that CXRO uses for their index of refraction values.

In a paper Steve Turley completed right before his retirement he found an issue with the well-known equation 23, stating that there were circumstances where it could be incorrect. This would be a very large development and have large effects in the world of optics. The paper was not peer reviewed, but the model he had almost completed working on is called MatR. The program follows his mathematics and calculations from that paper [27, pp. 16-17].

3.7 Conclusion

In conclusion, the main findings of this work include exploring the use of variable-angle of incidence "transmission" data to obtain optical constants. Previously, variable-angle of incidence *reflection data* has been fit and studied. However, in my study, I focused on learning how to fit thicknesses and optical constants using the output signal obtained from XUV

photodiodes. Through my modeling, I found that there is most likely major deviance from the literature values of the indices of refraction for SiO_2 and AlF_3 at the longer wavelengths of the XUV. In a three-material model using Fresnel coefficients, I was able to find values for the indices of refraction for these longer wavelengths through close fits to the data. These values differed from the literature values by over 25%. The thicknesses obtained using Beer's Law were not constant with wavelength. They were smaller at the longer wavelengths than those from data made at wavelengths near the Si L band edge. One interpretation is that the literature-derived indices of refraction of AlF_3 and SiO_2 are not suitable for these materials. Normalization of transmission data is a challenge. There can be a marked difference between measured and computed transmission at lower angles if this is not done well. The difference arises mostly clearly below the angle of total external reflection for the optical constants in the computation.

3.8 Future Work

This report was just the beginning of developing a method in order to find better values of the index of refraction of AlF_3 and SiO_2. Using the method developed, more data could be taken over more wavelengths to get a larger sample of data to work with to verify the results of this paper. Future students could use more data and better preliminary models to get better values for both the active and dead layer of the SiO_2. These values can then help to be able to model the layers with the AlF_3 later and extract those parameters.

Another aspect that needs to be examined from this study is the "I_0" parameter that was used in the fittings. This is a factor that is multiplied by the model of Equation 48. This factor seems to be able to scale up the data, but we are not entirely sure how it can affect the absorption.

Another very important further study is the study the equations derived by Dr. Turley and go to the ALS to test the accuracies of that model [27]. The implications of the physics involved in the models used are different than other optics texts and could be used in the development of the future of optics.

It would help the future of this project and the implications by testing and reviewing that paper's new information and using Steve Turley's updated code of MatR to model the next set of data that could not be completed in this project. By using the MatR code that can compute complete a similar model through as many layers as desired, this code could help find the optical properties of AlF_3 as this project originally intended to do

References

[1]   Thor Labs, "Optical Mirrors," ThorLabs, Inc, 2021. [Online]. Available: https://www.thorlabs.com/navigation.cfm?guide_id=15&gclid=Cj0KCQjw24qHBhCnA RIsAPbdtlLOk9RHEyBI_4XqiH1j2b1- QA0b11D5UoiTLWEe5gpeccScgfYQu1oaAo95EALw_wcB. [Accessed 9 July 2021].

[2]   B. Mellish, "Metal Reflectance," 19 November 2013. [Online]. Available: https://en.wikipedia.org/wiki/Reflectance#/media/File:Image-Metal-reflectance.png. [Accessed 1 July 2021].

[3]   D. M. Lewis, C. M. Plewe, A. G. Stapley, J. J. Vawdrey, R. S. Turley and D. D. Allred, "Illuminating the degradation of lithium fluoride mirror coatings in humid environments," *Proc. SPIE Advances in Optical and Mechanical Technologies for Telescopes and Instrumentation IV, 1145141,* vol. 11451, 2020.

[4]   W. Kesler, "The Chemistry of Corrosion Protection and Anti-Corrosion Coatings," Prospector, 29 September 2017. [Online]. Available: https://knowledge.ulprospector.com/7145/pc-corrosion-protection-chemistry-and-anti- corrosion-coatings/. [Accessed 1 May 2021].

[5]   Wikipedia, "Ultraviolet astronomy," Wikipedia, 14 May 2021. [Online]. Available: https://en.wikipedia.org/wiki/Ultraviolet_astronomy. [Accessed 2021 May 2021].

[6]   Edmund Optics, "Figure 2: EUV radiation falls between the X-ray and ultraviolet spectral regions," Edmund Optics Inc, Barrington, NJ, 2021.

[7]   D. D. Allred, R. S. Turley, S. M. Thomas, S. G. Willtt, M. J. Greeburg and S. B. Perry, "Adding EUV reflectance to aluminum-coated mirrors for space-based observation," *SPIE,* vol. 10398, no. UV/Optical/IR Space Telescopes and Instruments: Innovative Technologies and Concepts VIII, 103980Y, 5 September 2017.

[8]   D. D. Allred, R. S. Turley, S. M. Thomas, S. G. Willett, M. J. Greeburg and S. B. Perry, "Adding EUV reflectance to aluminum-coated mirrors for space-based observation," *Spie Digital Library,* vol. Proceedings Volume 10398, no. 1, p. 2, 2017.

[9]   LibreTexts, "Bond Polarity and Bond Strength," 3 December 2020. [Online]. Available: https://chem.libretexts.org/@go/page/183292. [Accessed 28 April 2021].

[10]   LibreTexts, " Table of Pauling electronegativities," 2020.

[11]   The European Synchrotron, "What is a Synchrotron?," The European Synchrotron, [Online]. Available: https://www.esrf.fr/about/synchrotron- science/synchrotron#:~:text=A%20synchrotron%20is%20an%20extremely,changes%20 direction%2C%20it%20emits%20energy.. [Accessed 20 May 2021].

[12]   Berkeley Lab, "About the ALS," Lawrence Berkeley National Laboratory, 2021. [Online]. Available: https://als.lbl.gov/about/about-the-als/. [Accessed 5 April 2021].

[13]   Advanced Light Source, "Machine Information," Lawrence Berkeley National Laboratory, 2021. [Online]. Available: https://als.lbl.gov/machine-information/. [Accessed 12 July 2021].

[14]   Today at Berkeley Lab, " What the Heck is a Beamline (and why is it important)?," Lawrence Berkeley National Laboratory, 14 May 2004. [Online]. Available: https://www2.lbl.gov/Science-Articles/Archive/tabl-wonder.html. [Accessed 12 July 2021].

[15]   E. Gullikson, "Beamline 6.3.2," Lawrence Berkeley National Laboratory, 2021. [Online]. Available: https://als.lbl.gov/beamlines/6-3-2/. [Accessed 13 July 2021].

[16]   MicroWorlds, "The Advanced Light Source—A Tool for Solving the Mysteries of Materials," MicroWorlds, [Online]. Available: https://www2.lbl.gov/MicroWorlds/ALSTool/. [Accessed 15 June 2021].

[17]   J. Hennessy, A. D. Jewell, K. Balasubramanian and S. Nikzad, "Ultraviolet optical properties of aluminum fluoride thin films deposited by atomic layer deposition," *Journal of Vacuum Science & Technology A,* vol. 34, no. 1, pp. 1-3, 2016.

[18]   B. D. Smith, "Reflectance Measurements of Two Thin Materials," B.S Thesis Brigham Young University, Provo, 2015.

[19]   M. Miles, "Evaporated Aluminum Fluoride as a Barrier Layer to Retard Oxidation of Aluminum Mirrors," Brigham Young University, Master's Thesis, Provo, 2017.

[20]   K. Fronk, "Storage of Al/AlF3 Thin-Film Mirrors in 327 K Oven," Brigham Young University Senior Thesis, Provo, 2021.

[21]   A. Davis, "Oxidation of Aluminum Under Various Thicknesses of Aluminum Fluoride," B.S. Thesis, Brigham Young Universty , Provo, 2018.

[22]   Wikipedia, "Beer–Lambert law," Wikipedia, 9 June 2021. [Online]. Available: https://en.wikipedia.org/wiki/Beer%E2%80%93Lambert_law. [Accessed 13 July 2021].

[23]   Zygomatic, "Diagram Editor," Zygomatic, [Online]. Available: https://www.diagrameditor.com/. [Accessed 5 Aug 2021].

[24]   J. Peatross and . M. Ware, "The Fresnel Coefficients," in *Physics of Light and Optics*, Provo, Brigham Young University, 2015, p. 78.

[25]   Wikipedia, "Propagation constant," 11 October 2021. [Online]. Available: https://en.wikipedia.org/wiki/Propagation_constant. [Accessed 18 October 2021].

[26]   Wikipedia, "Total external reflection," Wikipedia, 11 May 2020. [Online]. Available: https://en.wikipedia.org/wiki/Total_external_reflection. [Accessed 2022 March 24].

[27]   Z. Hughes, "Determining the Index of Refraction of Aluminum Fluoride in the Ultra Violet Spectrum," *BYU Scholars Archive,* vol. All Student Publications, no. 187, 2016.

[28]   R. S. Turley, "Transmission into an Absorbing Medium," *BYU Scholars Archive,* 2021.